AFRL-RV-HA-TR-2008-1150

Dynamically Resolved Simulation of Atmospheric Features and Turbulence Using Advanced Models and Adaptive Algorithms

D. Scott McRae
Hassan A. Hassan
Xudong Xiao

North Carolina State University
Department of Mechanical and Aerospace Engineering
Box 7910
Raleigh, NC 27695-7910

Final Report

30 October 2008

20090901188

AIR FORCE RESEARCH LABORATORY
AIR FORCE MATERIEL COMMAND
Space Vehicles Directorate
29 Randolph Rd.
Hanscom AFB, MA 01731-3010

AFRL-VS-HA-TR-2008-1150

Using Government drawings, specifications, or other data included in this document for any purpose other than Government procurement does not in any way obligate the U.S. Government. The fact that the Government formulated or supplied the drawings, specifications, or other data, does not license the holder or any other person or corporation; or convey any rights or permission to manufacture, use, or sell any patented invention that may relate to them.

This report is published in the interest of scientific and technical information exchange and its publication does not constitute the Government's approval or disapproval of its ideas or findings.

This technical report has been reviewed and is approved for publication.

/ signed /   / signed /
George Y. Jumper   Domenic F. Thompson, Maj, USAF, Chief
Contract Manager   Battlespace Surveillance Innovation Center

This report has been reviewed by the ESC Public Affairs Office (PA) and is releasable to the National Technical Information Service (NTIS).

Qualified requestors may obtain additional copies form the Defense Technical Information Center (DTIC). All other requestsors should apply to the National Technical Information Service (NTIS)

If your address has changed, if you with to be removed from the mailing list, or if the addressee is no longer employed by your organization, please notify AFRL/RVIM, 29 Randolph Rd., Hanscom AFB, MA 01731-3010. This will assist us in maintaining a current mailing list.

REPORT DOCUMENTATION PAGE

Form Approved
OMB No. 0704-0188

1. REPORT DATE (DD-MM-YYYY) 09-30-2008	2. REPORT TYPE Contract - Final	3. DATES COVERED (From - To) 06-17-2004 to 09-30-2008

4. TITLE AND SUBTITLE		
Dynamically Resolved Simulation of Atmospheric Features and Turbulence Using Advanced Models and Adaptive Algorithms	5a. CONTRACT NUMBER FA8718-04-C-0019	
	5b. GRANT NUMBER N/A	
	5c. PROGRAM ELEMENT NUMBER N/A	

6. AUTHOR(S)		
D. Scott McRae, Hassan A. Hassan, and Xudong Xiao	5d. PROJECT NUMBER 1010	
	5e. TASK NUMBER 0T	
	5f. WORK UNIT NUMBER A1	

7. PERFORMING ORGANIZATION NAME(S) AND ADDRESS(ES)	8. PERFORMING ORGANIZATION REPORT NUMBER
North Carolina State University Department of Mechanical and Aerospace Engineering Box 7910 Raleigh, NC 27695-7910	

9. SPONSORING / MONITORING AGENCY NAME(S) AND ADDRESS(ES)	10. SPONSOR/MONITOR'S ACRONYM(S) AFRL/RVBYA
Air Force Research Laboratory 29 Randolph Rd. Hanscom AFB, MA 01731-3010	
	11. SPONSOR/MONITOR'S REPORT NUMBER(S) AFRL-RV-HA-TR-2008-1150

12. DISTRIBUTION / AVAILABILITY STATEMENT

Approved for Public Release; Distribution Unlimited.

13. SUPPLEMENTARY NOTES

14. ABSTRACT

In order to resolve atmospheric features, such as gravity waves to the degree necessary for accurate optical turbulence prediction, we developed an adaptive version of MM5 that incorporates the NCSU Dynamic Solution Adaptive Grid Algorithm (DSAGA) and a new four-equation hybrid LES/RANS turbulence model that provides a new approach for the calculation of the index of refraction structure function Cn2, a quantitative measure of atmospheric optical turbulence. These four equations are used to model the turbulence kinetic energy, the variance of vorticity, the variance of potential temperature and its dissipation rate, respectively. The improvement in prediction of optical turbulence by the adaptive MM5 is documented by comparison with the models of Dewan and Jackson applied to unmodified MM5 output. By comparison with two sets of observations, the numerical results suggest that the adaptive MM5 Cn2 predictions approach binned observation variation in regions where the resolution has been improved by DSAGA, with little additional computational resources. However, predictions in both adaptive and fixed grid modes are degraded due to the fact that NWP codes, such as MM5, contain multiple types of numerical dissipation and in general use sponge layers at the upper boundary.

15. SUBJECT TERMS
Optical turbulence, dynamic solution adaptive mesh, hybrid LES/RANS turbulence model

16. SECURITY CLASSIFICATION OF:			17. LIMITATION OF ABSTRACT	18. NUMBER OF PAGES	19a. NAME OF RESPONSIBLE PERSON Dr. George Jumper
a. REPORT UNCLASSIFIED	b. ABSTRACT UNCLASSIFIED	c. THIS PAGE UNCLASSIFIED	UNLIMITED	38	19b. TELEPHONE NUMBER (include area code)

Standard Form 298 (Rev. 8-98)
Prescribed by ANSI Std. Z39.18

Table of Contents

Figures

Acknowledgments

Abbreviations and Acronyms

AFRL	Air Force Research Laboratory
AIAA	American Institute of Aeronautics and Astronautics
ARW	Advanced Research WRF
CFD	Computational fluid dynamics
DOD	Department of Defence
DSAGA	Dynamic solution adaptive grid algorithm
LES/RANS	Large eddy simulation/Reynolds averaged Navier-Stokes
MM5	Mesoscale Model 5
NASA	National Air and Space Administration
NCSU	North Carolina State University
NCSU k-ζ	A specific NCSU turbulence model
NWP	Numerical weather Prediction
PBL	Planetary boundary layer
PPM	Piecewise parabolic method
SGS	Subgrid scale
TKE	Turbulent kinetic energy
UTC	Universal Time, Coordinated
WENO	Weakly essentially non-oscillatory
WRF	Weather Research and Forecasting model

1. Summary

The goal of Phase 1 of this research was to complete development and verification of, as a proof of concept, an adaptive version of the community Fifth-Generation NCAR/Penn State Mesoscale Model MM5 including a coupled advanced hybrid Large Eddy Simulation/Reynolds-Averaged Navier-Stokes (LES/RANS) turbulence model for direct prediction of optical scale turbulence. Upon successful completion of Phase I, the adaptive and turbulence algorithms developed and installed in MM5 were to be installed in the Advanced Research version of the next-generation mesocale prediction Weather Research and Forecasting model (WRF-ARW) and also verified using standard reference cases. This report describes progress toward these goals and will describe the technical advances and accomplishments.

In order to resolve atmospheric features, such as gravity waves, to the degree necessary for accurate optical turbulence prediction and to ensure maximum benefit from the advanced hybrid LES-RANS turbulence model, the Euler equations in MM5 are transformed to a general curvilinear coordinate system and the NCSU dynamic solution adaptive grid algorithm (DSAGA) is installed. This adaptation algorithm reduces grid spacing locally by adjusting the position of grid nodes without increasing the total number of nodes in the grid. This method of adaptation is usually referred to as r- refinement. The node relocation is in response to a user-defined weight function distribution calculated from user selected features of the solution Grid adaptation is available in the entire domain when nesting is not used, in the entire lowest nest or in a subset of the lowest nest.

A four-equation hybrid LES/RANS turbulence model has been developed and incorporated into MM5 to provide a new approach for the calculation of the index of refraction structure function C_n^2, a quantitative measure of atmospheric optical turbulence. These four equations are used to model the turbulence kinetic energy (k), the variance of vorticity (ζ), the variance of potential temperature ($\widetilde{\theta''^2}$) and its dissipation rate (ϵ_θ), respectively.

The improvement in prediction of optical turbulence by incorporating DSAGA and the hybrid LES/RANS model in MM5 is documented by comparison with the models of Dewan and Jackson applied to unmodified MM5 output. By comparison with two sets of observations, the numerical results suggest that the adaptive MM5 C_n^2 predictions approach binned observation variation in regions where the resolution has been improved by DSAGA, with little additional computational resources. Selected comparisons are included in the results section.

The development and verification of the adaptive MM5 is documented in three proceedings publications (References 1–3) and in an article accepted for publication in the AIAA journal (Reference 4). Reviews of the research were given at three AIAA Aerospace Sciences Meetings, one American Meteorological Society meeting, and three workshops, two at

Hanscom AFB and one at Arizona State University.

The NCSU personnel who participated in this project were D. Scott McRae, Professor, PI; Hassan A. Hassan, Professor, Co-PI; Xudong Xiao, Research Assistant Professor, Code Developer; and Yih-Pin Liew, Post-Doctoral Research Associate, code developer.

The second phase of the project to install DSAGA and the hybrid model in WRF-ARW was not complete at project termination. The primary code developer, Dr. Xiao, left the project just as work began on the WRF version. Due to few current doctoral graduates with high-level CFD code development skills, compounded by visa restrictions for some otherwise qualified candidates, eleven months and an international search were required to find and employ a qualified replacement for Dr. Xiao. Although the WRF version is not complete, development is being continued under separate DOD funding and will therefore be available for operational use when completed.

2.   Introduction

Atmospheric optical turbulence refers to the range in the turbulence spectra in the atmosphere that causes significant fluctuations in the refractive index of air. These fluctuations affect the propagation of optical signals and images by random refraction which can result in a reduction of optical signal effective power, range, and coherence, and can also degrade image quality. The primary sources of high altitude atmospheric optical turbulence are gravity wave breaking and jet streams. Gravity waves arise from a number of sources including topography, convection, and wind shear. The turbulence layers resulting from these gravity waves have thicknesses of the order of tens of meters and may extend for many kilometers in the horizontal direction.

As noted by Jumper and Beland (Reference 5), considerable observational effort has been expended with the goal of expanding available databases of the refractive index in the atmosphere, and average profiles have been obtained for selected locations. However, measuring directly the detailed state of the atmosphere for a wide range of conditions, locations and times is not practical. Thus, there is a need to develop simulation tools needed to predict optical turbulence for given initial and boundary conditions. These simulation tools can then be initialized with local conditions and observations and used to provide tactically useful predictions to meet DOD requirements.

Examination of optical turbulence predictions obtained by post processing C_n^2 distribution from the output of current mesoscale numerical weather prediction (NWP) codes reveals two fundamental problems. First, the numerical resolution is not adequate to resolve gravity waves or the scales of optical turbulence. Second, the optical turbulence parameterization via Tatarskii (C_n^2) is based on methods developed for Large Eddy Simulation (LES) scale

2

resolution and thus is not well suited for the much coarser mesoscale model resolution. Both of these NWP code problems are addressed in the current work: first, by installing a dynamic solution adaptive grid algorithm (DSAGA) to improve resolution of the atmospheric phenomena leading to optical turbulence and second, by extending a physically derived turbulence closure (the NCSU k-ζ model) to provide directly the structure functions required to predict optical turbulence. Both of these techniques were developed for aerospace applications under DOD and NASA funding. The modification of these techniques for NWP use is a technology transfer example and is an unanticipated benefit resulting from the original research funding. Progress in the application and further development of these advanced techniques for optical turbulence prediction has been reported in contract reports, and in proceedings and an article by Xiao, et al (References 1–4).

The index of refraction structure function, C_n^2, is the most relevant quantity for optical propagation predictions. Current practice for the calculation of C_n^2 employs mesoscale NWP codes, such as MM5 (Reference 6). These codes forecast relevant atmospheric quantities such as wind velocity, temperature, relative humidity, etc., on typical grid spacings in the range 4–30 km in the horizontal direction and 0.3–1.0 km in the vertical direction. The vertical spacing is further refined in the planetary boundary layer (PBL). As indicated earlier, optical turbulence scales are of the order of tens of meters. Therefore, a parameterization of C_n^2 is employed, which gives C_n^2 in terms of flow properties output from the specific mesoscale weather prediction code being used.

The expression for C_n^2 for optical wavelengths near the visible range is given by (References 7,8)

$$C_n^2 = \left(76 \times 10^{-8} \frac{P}{\theta T} \right)^2 C_\theta^2 \tag{1}$$

where P is the pressure, in Pascals, T and θ are the temperature and potential temperature, respectively, in degrees Kelvin, and

$$C_\theta^2 = a^2 \epsilon_\theta / \epsilon^{1/3}, \quad a^2 = 2.8 \tag{2}$$

where ϵ_θ is the dissipation rate of the variance of potential temperature and ϵ is the dissipation rate of the variance of velocity or turbulent kinetic energy (TKE).

The parameterization developed by Tatarskii (Reference 7) serves as the basis for current statistical models. According to his theory, C_θ^2 can be expressed as

$$C_\theta^2 = 2.8 L_0^{4/3} \left(\frac{\partial \theta}{\partial z} \right)^2 \tag{3}$$

where L_0 is the "outer length scale" and z is the vertical direction. Current statistical models (References 9, 10) attempt to parameterize L_0 in terms of altitude and/or velocity and potential temperature gradients. On the other hand, Jackson's model (Reference 11) uses the temperature lapse rate $(\partial T/\partial z)$ to parameterize L_0 because it provides better correlation with thermosonde data. Other models were developed by Bougeault et al. (Reference 12) and Tunick (Reference 13) for use in the PBL. Currently, a common procedure is to use outputs from mesoscale models as inputs to the above models to calculate C_n^2.

In order to avoid the set of simplifying assumptions that led to Eq. (3) and current models (References 9–13), the Euler equations in MM5 are supplemented by the TKE and an equation for its dissipation rate, $\nu\zeta$, where ν is the kinematic viscosity and ζ is the variance of vorticity, or enstrophy (Reference 14); and an equation for the variance of potential temperature, $\widetilde{\theta''^2}$, and its dissipation rate, ϵ_θ (Reference 15). These four equations were derived directly from the full Navier-Stokes equations and thus retain true relevant physics. As a result, it is now possible to calculate C_n^2 from Eqs. (1) and (2) without further simplifying assumptions. Further, in order to account for the scales that are not resolved by LES, a hybrid Large Eddy Simulation/Reynolds Averaged Navier-Stokes (LES/RANS) solver (Reference 16) has been incorporated into MM5. The RANS model provides the desired subgrid scale model needed in LES calculations.

In order to resolve atmospheric features, such as gravity waves, to the extent necessary for accurate optical turbulence prediction and to ensure maximum benefit from the advanced hybrid LES-RANS turbulence model, the Euler equations in MM5 are transformed to a general curvilinear coordinate system and the NCSU dynamic solution adaptive grid algorithm (DSAGA) is installed. This r- refinement algorithm reduces grid spacing locally in response to a user-defined weight function distribution calculated from selected features of the solution and does so without increasing the total number of nodes in the grid.

The remainder of this report gives the technical details of the implementation of DSAGA and the hybrid model, and compares example predictions with observations carried out at Holloman Air Force Base. Conclusions are drawn and recommendations made for future work.

3. Technical Approach and Modifications to MM5

3.1. Governing Equations and Transformations

The non-hydrostatic governing equations in MM5 (Reference 6), defined in the x, y, σ coordinate system, are transformed in all three dimensions to a uniform computational coordinate system, using the chain-rule according to:

$$
\begin{aligned}
\tau &= t \\
\xi_i &= \xi_i(x, y, \sigma, t), \quad i = 1, 2, 3
\end{aligned}
\tag{4}
$$

where σ is the nondimensional pressure coordinate. The resulting equations have the form

$$
\frac{\partial \mathbf{U}}{\partial \tau} + \frac{\partial \mathbf{U}}{\partial \xi_i}\frac{\partial \xi_i}{\partial t} + m^2\frac{\partial \mathbf{E}}{\partial \xi_i}\frac{\partial \xi_i}{\partial x} + m^2\frac{\partial \mathbf{F}}{\partial \xi_i}\frac{\partial \xi_i}{\partial y} + \frac{\partial \mathbf{G}}{\partial \xi_i}\frac{\partial \xi_i}{\partial \sigma} = \mathbf{S}
\tag{5}
$$

where

$$
\begin{aligned}
\mathbf{U} &= [p^*p', p^*u, p^*v, p^*w, p^*T]^T, \\
\mathbf{E} &= \frac{u}{m}[p^*p', p^*u, p^*v, p^*w, p^*T]^T, \\
\mathbf{F} &= \frac{v}{m}[p^*p', p^*u, p^*v, p^*w, p^*T]^T, \\
\mathbf{G} &= \dot{\sigma}[p^*p', p^*u, p^*v, p^*w, p^*T]^T,
\end{aligned}
\tag{6}
$$

m is the map scale, p^* the reference pressure, and p' the pressure perturbation, T the temperature, and u, v and w are velocity components in the x-, y-and z-direction, respectively. All other terms, such as pressure gradient, Coriolis force, and gravity terms are included in $\mathbf{S}$; see Reference 6 for more details. The above equations are discretized in the Arakawa-B (Reference 17) type staggered grid, using the same finite difference stencils as MM5, e.g., the stencils used in the x-direction in MM5 are applied to the ξ_1 direction here. These equations are also solved using the leap-frog scheme. In order to obtain accurate discretization in the curvilinear staggered grid, three sets of metric derivatives are calculated to be consistent with the differencing of flow variables. The variables and metric derivatives are defined at three different locations: the cell center for p' and T, the center of cell edges for u and v and the center of cell surface for w and $\dot{\sigma}$.

In MM5, in order to remove the limitation on the time step due to small mesh spacing in

the vertical direction, the following two coupled equations for w and p' are solved implicitly:

$$\frac{\partial w}{\partial t} - \frac{\rho_0 g}{\rho p*} \frac{\partial p'}{\partial \sigma} + \frac{g}{\gamma} \frac{p'}{p} = S_w \tag{7}$$

$$\frac{\partial p'}{\partial t} - \frac{\rho_0 g \gamma p}{p*} \frac{\partial w}{\partial \sigma} - \rho_0 g w = S_{p'} \tag{8}$$

This results in a tridiagonal system along the σ-direction for w in the uniform mesh, which can be solved directly. In the computational plane, the σ variation is transformed as $\partial_\sigma = \xi_{i,\sigma} \partial_{\xi_i}$, where $\xi_{i,\sigma}$ stands for $\frac{\partial \xi_i}{\partial \sigma}$. Therefore, Eqs. (7) and (8) must be solved iteratively. The iteration scheme chosen is as follows:

1. $p'^{(0)} = p'^t$, $w^{(0)} = w^t$;

2. solve the following system iteratively:

$$\frac{w^{(i+1)} - w^t}{\Delta t} - \frac{\rho_0 g}{\rho p*} \left(\frac{\partial p'}{\partial \xi_3}\right)^{(i+1)} \xi_{3,\sigma} + \frac{g}{\gamma} \frac{p'^{(i+1)}}{p} = S_w + \frac{\rho_0 g}{\rho p*} \left[\left(\frac{\partial p'}{\partial \xi_1}\right)^{(i)} \xi_{1,\sigma} + \left(\frac{\partial p'}{\partial \xi_2}\right)^{(i)} \xi_{2,\sigma}\right] \tag{9}$$

$$\frac{p'^{(i+1)} - p'^t}{\Delta t} - \frac{\rho_0 g \gamma p}{p*} \left(\frac{\partial w}{\partial \xi_3}\right)^{(i+1)} \xi_{3,\sigma} - \rho_0 g w^{(i+1)} = S_{p'} + \frac{\rho_0 g \gamma p}{p*} \left[\left(\frac{\partial w}{\partial \xi_1}\right)^{(i)} \xi_{1,\sigma} + \left(\frac{\partial w}{\partial \xi_2}\right)^{(i)} \xi_{2,\sigma}\right] \tag{10}$$

3. when converged, $p'^{t+1} = p'^{(i+1)}$ and $w^{t+1} = w^{(i+1)}$

where t and $t+1$ denotes two time levels, respectively, "(0)" the initial values and i the number of iterations. For simplicity, $p'^{(i)}$ and $w^{(i)}$ are used to illustrate the algorithm. However, they are implemented as an averaged value of $p'^{(i)}$ and p'^t , and $w^{(i)}$ and w^t, respectively (Reference 6). Note that Eqs. (9) and (10) are in a form similar to Eqs. (7) and (8) so that the tridiagonal solver can be applied to the ξ_3-direction. To implement this semi-implicit solver in transformed space, an outer loop is added to the original MM5 loop to update the right hand side of the above equations.

3.2. The Dynamic Solution Adaptive Grid Algorithm (DSAGA)

The DSAGA adaptive grid algorithm as currently installed in the MM5 is a modification of the NCSU developed algorithm and was first described in Reference 1. In order to install the adaptive grid algorithm, the non-hydrostatic governing equations in MM5 defined in the x, y, σ coordinate system are transformed to a general curvilinear coordinate system. The resulting equations were discretized in the Arakawa-B (Reference 17) staggered grid and solved using the leap-frog scheme. Since the flow properties are stored at three different locations in the Arakawa grid, three sets of grid metric derivatives are calculated that define the transformation to the curvilinear grid as noted in the preceding section. The DSAGA algorithm then performs r-refinement adaptation in order to increase resolution of solution features by relocating grid nodes in a solver-independent manner. A weight function, based on user-selected solution properties, is calculated and then used in a center of mass scheme to control the grid node relocation. In the work presented here, the weight function is based on the distribution of the magnitude of vorticity:

$$W = |\nabla \times \vec{V}|, \tag{11}$$

where $\vec{V}$ is the velocity vector. As has been shown in Reference 1, this weight function is a good indicator for gravity wave-breaking and also is significant in other regions of large shear. The weight function due to vorticity associated with each cell is treated as the mass of the cell. Then the center-of-mass algorithm determines the new grid by clustering nodes where the magnitude of vorticity is large, thereby increasing resolution in regions of large shear (c.f. Reference 1) for details. The basic grid adaptation procedure using DSAGA can be outlined as follows:

1. Calculate the weight function using Eq(11).

2. Restrict the weight function by

$$W = \min(\max(W, a_1 W_{ave}), a_2 W_{ave}) \tag{12}$$

   where W_{ave} is the average value of W in the entire domain and a_1 and a_2 are two coefficients that prescribe the floor and ceiling values of the weight function, respectively. This reduces drastic grid node movements due to very large or very small weight functions.

3. Smooth the weight function using an elliptic smoother to reduce the "noise" in the weight function in order to obtain a grid with smoother distribution of cell volume.

Then rescale the resulting weight function based on an input max-to-min ratio in order to bias the relocation of the grid toward larger or smaller movement-.

4. Obtain the new grid displacement in the computational domain, $(\Delta\xi, \Delta\eta, \Delta\varsigma)$, using the center-of-mass algorithm.

5. Calculate the new grid node locations in the physical coordinate system, and redistribute the flow solutions to the new locations using a high order advection scheme.

By examining Eq(12), it is clear that this restriction tends to adjust the maximum and minimum value of the weight function according to the average of all weights, i.e., if the average of the weight functions are small, then both ceiling and floor value in Eq(12) are small. In practice, the values of a_1 and a_2 require careful tuning on a case by case basis. Therefore, isolated high vorticity regions may not influence the function sufficiently using this approach. Since the purpose of this "restriction" is to remove too large and too small values, a new approach based on the n-th largest value search (Reference 18) is employed:

$$W = \min(\max(W, W_{n_1\%}), W_{n_2\%}), \tag{13}$$

where $W_{n_1\%}$ ($W_{n_2\%}$) is a weight function value that is greater than $n_1\%$ ($n_2\%$) of population and less or equal than the rest, and $n_1 < n_2$. In a sequential mode, the cost of this searching algorithm, in terms of both time and memory, is proportional to the number of grid nodes, so it is as efficient as the approach in Eq(12). Using this approach, the floor and the ceiling values are not dependent on the average value, and it can guarantee that there are $(n_2 - n_1)\%$ of weight functions unaffected by this restriction procedure.

In the solver independent version of DSAGA, as applied here, the grid relocation process determines the grid distribution such that it improves resolution of the solution as an initial condition for the next solver step. However, the solution on which this relocation is based is defined only on the previous grid. A conservative advection scheme is then used to redistribute the solution to the new grid nodes. This step is crucial for preserving the accuracy of the solution and for realizing the benefit of the relocation.

In the solution redistribution step, an advection equation is solved for each flow variable. The first scheme used for this task was a WENO (Reference 19) based scheme that tended to smooth the solution and thereby did not provide the required redistribution accuracy. A modified Piecewise Parabolic Method(PPM) scheme, developed by Rider *et al* (Reference 20), was adopted to increase redistribution accuracy. In the PPM framework, the single time step scheme can achieve third order accuracy in both the temporal and the spatial directions due to integration over a constructed parabola within grid cells. Therefore it is more efficient than the multi-step WENO scheme. In Rider's approach, the base PPM

(Reference 21) is combined with WENO and high order (non-monotone) schemes. A median function is employed to select the optimal cell edge values for constructing the parabola in the cell. This approach maintains uniformly high order accuracy, even at extrema. A slight change was made on the high order component to simplify the implementation, while maintaining similar accuracy. Instead of a 6 point stencil as in Reference 20, the following 4-point stencil is used for the edge value:

$$\phi_{j+1/2} = \frac{7}{12}(\phi_j + \phi_{j+1}) - \frac{1}{12}(\phi_{j+2} + \phi_{j-1}) \tag{14}$$

where the ϕ is the variable of interest.

3.3. Turbulence Closure

3.3.1. Review of Tatarskii's Theory

In order to contrast the proposed approach with existing approaches, a brief review of Tatarskii's theory is presented. Tatarskii assumed that turbulence exists in a state of equilibrium and that the Richardson number is zero. The first assumption requires that production and dissipation rates of TKE and $\widetilde{\theta''^2}$ are equal, while the second ignores the contribution of gravity to the above terms. Thus, the above assumptions yield

$$\epsilon = \nu_t \left(\frac{\partial u_i}{\partial x_j}\right)^2 \approx \nu_t \left(\frac{\partial u}{\partial z}\right)^2 \tag{15}$$

and

$$\epsilon_\theta = \alpha_t \left(\frac{\partial \theta}{\partial x_i}\right)^2 \approx \alpha_t \left(\frac{\partial \theta}{\partial z}\right)^2 \tag{16}$$

where ν_t and α_t are the turbulent eddy viscosity and turbulent diffusivity. Using Eqs. (15) and (16), Eq. (2) reduces to

$$C_\theta^2 = a^2 \left(\frac{\alpha_t}{\nu_t}\right) \left[\frac{\nu_t^2}{\left(\frac{\partial u}{\partial z}\right)^2}\right]^{1/3} \left(\frac{\partial \theta}{\partial z}\right)^2 \tag{17}$$

The next assumption of Tatarskii pertains to ν_t and α_t. He assumed that ν_t is determined from the mixing length theory of Prandtl, i.e.,

$$\nu_t = l_{mix}^2 \left|\frac{\partial u}{\partial z}\right| = L_0^2 \left|\frac{\partial u}{\partial z}\right| \tag{18}$$

Moreover, he sets

$$\frac{\alpha_t}{\nu_t} \approx 1 \tag{19}$$

9

As a result of the above assumptions,

$$C_\theta^2 = 2.8 L_0^{4/3} \left(\frac{\partial \theta}{\partial z} \right)^2 \tag{20}$$

Existing statistical models (References 9–11) of optical turbulence differ by the manner in which L_0 is modeled. It is chosen as a function of one or more of $\frac{\partial u}{\partial z}$, $\frac{\partial \theta}{\partial z}$, $\frac{\partial T}{\partial z}$ and z.

3.3.2. The Hybrid LES/RANS Turbulence Model

In this work, the turbulence is modeled using a hybrid LES/RANS model. The four equation k-ζ model, which is an extension of the standard two-equation k-ζ model (Reference 14), serves as the RANS component. The four equations account for the turbulence kinetic energy (TKE) or the velocity variance, k, the variance of vorticity or enstrophy, ζ, which provides the dissipation rate ($\epsilon = \nu \zeta$) for k, the variance of the potential temperature, $\widetilde{\theta''^2}$, and its dissipation rate, ϵ_θ. These four equations were derived from the exact Navier-Stokes equations and then modeled term by term so as to insure that relevant physics is reflected in the resulting model equations. The LES subgrid scale (SGS) model consists of the k-Δ and $\widetilde{\theta''^2}$-Δ models, where the Δ is the grid spacing in the vertical direction. The k-Δ model was a variant of the one equation model of Yoshizawa and Horiuti (Reference 22), which can recover a Smagorinsky model in LES regions when production balances dissipation in the absence of buoyancy effect. The current $\widetilde{\theta''^2}$-Δ takes a similar form as the k-Δ model. Inclusion of equations for $\widetilde{\theta''^2}$ and ϵ_θ makes it possible to calculate the turbulent thermal diffusivity as part of the solution. Thus, this model computes the turbulent Prandtl number directly.

The hybrid scheme results from the combination of the RANS and the LES components through a blending function (Reference 16), Γ, which blends the turbulent eddy viscosity, ν_t, turbulent thermal diffusivity, α_t, the k-equation, and the $\widetilde{\theta''^2}$-equation. The current blending function varies from 0 to 1. When $\Gamma = 0$, the hybrid model reduces to the RANS model, while $\Gamma = 1$ yields the LES limit. The advantage of this approach lies in the fact that all scales are taken into consideration. The scales that can be resolved are calculated directly, while the ones that cannot be resolved are modeled. If the resolution is insufficient for LES scales, the RANS model is used.

In this hybrid scheme, the dissipation rates for both variances consist of two components: one is due to the RANS model, and the other is due to the LES subgrid model. Therefore,

the resulting dissipation rates are expressed as

$$\epsilon_{hybrid} = (1 - \Gamma)\nu\zeta + \Gamma\frac{k^{3/2}}{\Delta} \tag{21}$$

$$\epsilon_{\theta,hybrid} = (1 - \Gamma)\epsilon_\theta + \Gamma C_{h,d}\frac{\widetilde{\theta''^2}^{5/4}\sqrt{C_p}}{\Delta} \tag{22}$$

where $\nu\zeta$ is the dissipation rate for k in the RANS component, $C_{h,d}$ is a model constant, and C_p is the specific heat at constant pressure. With these two dissipation rates, C_θ^2 can be directly calculated using Eq. (2), instead of using the simplifying assumptions noted previously.

In order to take the buoyancy effect into account, the heat flux $\widetilde{\theta'' u_j''}$, is modeled by

$$\widetilde{\theta'' u_j''} = -\alpha_t \left(\frac{\partial\tilde{\theta}}{\partial x_j} + C_{h,g}\frac{g\tau_\theta}{\tilde{\theta}}\delta_{j3}\widetilde{\theta''^2} \right), \tag{23}$$

where $C_{h,g}$ is a model constant, g is the gravity acceleration, and τ_θ is a time scale determined by $\widetilde{\theta''^2}$ and $\epsilon_{\theta,hybrid}$. The above approach is based on a similar modeling in Garratt's monograph (Reference 23).

The four model variables are initialized by assuming that the initial ν_t equals to the Smagorinsky eddy viscosity, $\nu_{t,LES} = \nu_{t,RANS}$ and $\nu_{t,LES} = \alpha_{t,RANS}$. The model equations are discretized and solved in the same fashion as the other equations in MM5. Zero-gradient lateral boundary conditions are used owing to the absence of k, ζ, $\widetilde{\theta''^2}$ and ϵ_θ from outer domains in the standard MM5. The model equations and model constants used are given in the Appendix. Details of the derivation and model constants are given in References 14 and 15.

4. Results and Discussion

Selected results are presented in this section to illustrate the improved C_n^2 forecast provided by the NCSU four equation hybrid LES/RANS turbulence model and the NCSU adaptive algorithm DSAGA as installed in the modified MM5. More complete results are available in Xiao, et.al. (Reference 1–4)

Three code configurations are used:

1. standard, unmodified MM5 with the standard MM5 turbulence modeling.

2. The adaptive MM5 with the four equation turbulence model executed in fixed, horizontally uniform, grid mode (referred to as "uniform" in figures).

3. The adaptive MM5 with the four equation turbulence model in full three dimensional adaptive mode. The installed capability to increase the number of levels independently in the adaptive domain was not exercised for these comparisons as the initial goal was to demonstrate benefit with little additional computational resources.

Two sets of thermosonde measurements were used during the project to provide observational comparisons. The first set consists of three thermosonde/radiosonde profiles collected in Oct 2001 at Vandenberg Air Force Base (Reference 24). The second set was collected in Oct 2003 at Holloman Air Force Base. Results for all three code configurations will be compared directly with the Holloman observation. Comparisons with the Vandenberg sets are included in Reference 2. Balloon number and launch time for these data are given in Table 1. The high-resolution observations along the balloon trajectory were binned at 500m vertical intervals for comparison with numerical results. In addition to the observational data, C_n^2 profiles obtained from Dewan's (Reference 10) and Jackson's models (Reference 11) using standard MM5 output (Reference 24) and using adaptive MM5 output are included in the comparisons. For these two models, the prediction depends solely on the velocity and temperature distributions that are computed by the standard MM5 or interactively computed by the modified MM5 using the hybrid LES/RANS model. Since the LES/RANS model interacts with the solution, the Dewan and Jackson results for C_n^2 produced by these two inputs will differ.

Table 1. Model Initialization time and Balloon Launch Time

	Model Initialization Time	Balloon #	Balloon Launch Time
Holloman Case	26-Oct-2003 1200 UTC	1	27-Oct-2001 0252 UTC

However, results obtained with either the modified or original MM5 cannot be expected to reproduce the binned thermosonde/radiosonde data even if nominal vertical spacing is

Table 2. Attributes of MM5 Grids in Holloman case

Nest	1	2	Adaptive
Horizontal Grid Spacing (km)	15	5	5 (initial)
Horizontal Grid Size (number of nodes)	109×109	163×163	123×123
Vertical Grid Size (Levels)	80		

similar to the binning range in the stratosphere. First, numerical dissipation is required to maintain stability of the MM5 computation and is also used to damp spurious acoustic modes, etc. The collective effect of these dissipations will tend to reduce the amplitude of (or even remove entirely) the higher frequencies resolved theoretically by the mesh spacing. Second, the absorptive layer condition used to cancel wave reflections at the upper computational boundary tends to damp frequencies in the upper stratosphere. These effects tend to smooth shear layers with the result that MM5 distributions of temperature and velocity used to obtain C_n^2 will have reduced variation and structure as compared with observation. This reduced variation will also influence the predictions obtained with the models of Jackson and Dewan, which depend on these distributions.

Both standard and adaptive MM5 inputs for mesh sizing, nesting and initial and boundary conditions for the Holloman case were those used previously by Ruggiero (Reference 24) for comparisons with observation using the standard MM5. The grid attributes for standard and adaptive MM5 domains are given in Table 2. The adaptive domain is nested in the inner standard MM5 domain (Domain 2), which provides lateral boundary conditions needed for the adaptive domain. Initial grid resolution in the adaptive domain, in both the horizontal and the vertical directions, is the same as that for Domain 2 as given in Table 2. The domain layout showing the relative location of the grid nest and adapted region is shown in Figure 1. The surface normal mesh distribution used by Ruggiero (Reference 24) results in approximately even 300m vertical spacing in the stratosphere. The MM5 initialization time for this case is 1200 UTC 26-Oct-2003.

During computation, grid relocation and the subsequent solution redistribution are conducted every three Domain 2 time steps. The time step in the adaptive domain is calculated temporally such that the adaptive solver uses the maximum time step that the CFL condition allows in order to advance to the same time level as in the outer standard MM5 domain. All C_n^2 resulting from the adaptive MM5 solver are calculated using the four-equation hybrid LES/RANS model described in Section 3.3.

In order to obtain profiles of C_n^2 and other quantities along the balloon trajectory, three dimensional flow field data were output every 10 minutes simulation time, and TECPLOT$^{\text{TM}}$was used to interpolate the solutions, spatially and temporally, to the trajectory. A snapshot of

13

two vertical grid surfaces from the three dimensional adaptive grid region, with the weight function contours superimposed, is shown in Figure 2. Note that none of the adapted grid surfaces are planar since the adaptation is fully three dimensional. The balloon trajectory is projected onto this snapshot so that the influence of the wind field is evident. As can be observed in this figure, grid nodes are clustered in regions of large weight function (high vorticity). In regions below z=4 km , the vorticity based weight function was set to the floor value (see Eq. 13) to allow concentration of adaptation in the upper atmosphere. This view could also have been superimposed with the local value of the C_n^2 prediction in order to indicate that the LES-RANS turbulence model gives this prediction everywhere for all model run times as a direct output.

Figure 3 shows a comparison of the potential temperature profiles, where good agreement is indicated. This figure also shows that the tropopause is located at $z \approx 11$ km. The adaptive grid algorithm weight function is biased in this case to provide more adaptation above the tropopause, where accurate prediction of C_n^2 is required for this application, and less below. The resulting grid is refined dynamically in the region between z $\approx$ 11 km and z $\approx$ 19 km, as indicated by grid spacing distribution in Figure 4. An earlier grid distribution using Eq. 12 (instead of Eq. 13) and the grid distribution used both in the unmodified, fixed grid MM5 and as input for the adaptive MM5 are included.

Figure 5 gives a comparison of C_n^2 obtained by Dewan's and Jacksons' models by use of output from the unmodified, fixed grid MM5 with that from direct output of C_T^2 from the current adaptive MM5 and the hybrid LES/RANS model. As a result of grid refinement, the adaptive MM5 C_n^2 profile shows more structure in the upper atmosphere and reproduces more closely the large C_n^2 variations shown in the binned observation which are absent from the Dewan's and Jackson's model predictions from the unmodified MM5.

Figure 6 compares the same adaptive LES/RANS C_n^2 profiles shown in Figure 5 with the adaptiveLES/RANS code in fixed grid mode (labeled as uniform). These results demonstrate that the C_n^2 prediction provided by the hybrid LES/RANS model is improved in both high and standard resolution grid modes. Figure 7 compares the meridional wind profiles for results shown in the previous Figures. The standard MM5 profile due to Ruggiero (Reference 24) is smooth, indicating that most strong wind shear was reduced by a combination of coarse grid spacing and dissipation in the standard MM5. The level of wind shear present in the binned observation is more closely approximated in the current adaptive results, indicating that the overall effective dissipation is reduced by adaptation and the four-equation turbulence model. The misalignment of extrema between the adaptive solution and the observational data may be due to the sponge layer on the upper boundary, which may cause a boundary layer like behavior near the top boundary and displace the extrema locations towards the surface. This misalignment of extrema is also apparent in the C_n^2 profiles.

14

Although it is clear from the above noted figures that the displacement of the results by the boundary condition implementations preclude any meaningful application of standard accuracy measures, examination of statistical measures may indicate progress toward the goal of direct verification. Table. 2 compares, quantitatively, the performance of different schemes in both low and upper atmosphere in terms of the mean and the standard deviation of C_n^2. The mean of C_n^2 is defined as:

$$\overline{C_n^2} \equiv \frac{1}{z_2 - z_1} \int_{z_1}^{z_2} C_n^2 dz, \tag{24}$$

and the standard deviation of C_n^2 is defined as

$$\sigma(C_n^2) \equiv \sqrt{\frac{1}{z_2 - z_1} \int_{z_1}^{z_2} (C_n^2 - \overline{C_n^2})^2 dz}, \tag{25}$$

where z_1 and z_2 are the lower and upper bounds of altitude. The mean describes the integral of C_n^2 through the air, which is an useful quantity in relevant calculations for optical propagation (Reference 9), while the deviation can be used to describe the variations of C_n^2. Note that the C_n^2 presented were collected along the balloon trajectory. However, numerical experiments show that no significant difference exists in these statistical measures between profiles along a vertical line through the observation site and along the actual trajectory, since the balloon trajectory crosses only a few grid cells horizontally. Therefore, we choose to integrate C_n^2 in the z-direction.

Table 3. Comparison of mean and standard deviation of C_n^2 at lower (4 km $< z <$ 10 km) and upper (10 km$\leq z <$20 km) atmosphere

Models	Lower Atmosphere		Upper Atmosphere	
	mean	σ	mean	σ
Observation	5.69×10^{-18}	5.77×10^{-18}	1.99×10^{-17}	3.52×10^{-17}
Dewan	2.74×10^{-17}	3.64×10^{-17}	7.61×10^{-18}	1.26×10^{-17}
Jackson	3.51×10^{-18}	4.60×10^{-18}	2.12×10^{-18}	1.34×10^{-18}
Current Adaptive	3.00×10^{-18}	3.06×10^{-18}	5.28×10^{-18}	9.84×10^{-18}
Previous Adaptive	4.77×10^{-18}	5.47×10^{-18}	3.73×10^{-18}	3.38×10^{-18}
Uniform	5.38×10^{-18}	5.80×10^{-18}	3.79×10^{-18}	3.17×10^{-18}

This table shows that, in the lower atmosphere, the current hybrid model on the uniform grid matches the C_n^2 mean more closely than Jackson's and Dewan's model. In the upper atmosphere below 20 km, above which level grid resolution is not sufficient to resolve wind shear, the current adaptive model results match more closely the observational mean and

15

deviation than the previous adaptive results and Jackson's model. Examination of the Dewan's model results indicates that the apparent improved agreement by this model is biased by a single peak between 11 km $< z <$ 14 km. The Dewan's model indicates considerably less structure than the adaptive model over the remainder of the range. When improved grid adaptation scheme is used, the grid refinement in the upper atmosphere improves the C_n^2 prediction over the previous grid adaptation scheme, which did not cause sufficient mesh refinement. But the mean C_n^2 in the lower atmosphere is reduced due to coarser resolution, caused by conservation of grid nodes, but the value still remains comparable to Jackson's model.

5.   Conclusion

The first goal of the research has been met by developing a proof-of-concept NWP code based on the well known MM5 that includes a new hybrid LES/RANS turbulence model developed at NCSU for C_n^2 prediction and by modifying MM5 for, and installing, a version of the NCSU 3-D dynamic solution adaptive grid algorithm DSAGA. The LES/RANS turbulence model extends the hybrid NCSU k–ζ model by adding two other model equations; one for the variance of potential temperature, and the other for its dissipation rate. Therefore the two critical quantities, ϵ and ϵ_θ, for calculating C_n^2 can be directly simulated without further simplification.

Optical turbulence predictions obtained by use of the new adaptive MM5 code, including the hybrid LES/RANS model, and of the unmodified MM5, with Dewan's and Jackson's models, have been compared with two sets of observations conducted at the Vandenberg and Holloman Air Force Bases and published in proceedings with sample results included herein for the Holloman case. The results show that the new hybrid model and the DSAGA adaptive algorithm combine to predict C_n^2 with variations and mean values that approach those in the binned observations, thereby providing more useful predictions for operational use as compared with information derived from the unmodified code. However, this conclusion must be qualified by noting that the adapted solution is not yet accurate in the usual sense (direct comparison with the raw balloon data) as the shear layers and other variations are displaced and reduced by boundary effects and dissipation in the code. When grid spacing is large, it was noted that an improved dissipation rate blending function for the two types of fluctuations should be explored in future investigations in order to improve the prediction, especially near the tropopause.

Predictions in both adaptive and fixed grid modes are degraded due to the fact that NWP codes, such as MM5, contain multiple types of numerical dissipation and, in general, use sponge layers at the upper boundary. Both of these features contribute to smoothing

of shear layers in the flow which then reduces variation in the prediction. This effect is reduced but not eliminated by adaptation of the grid. Further work with standard NWP codes should include efforts to reduce the amount and types of numerical dissipation in these codes.

The adaptive MM5 developed during this project is a research oriented code only, as further development was halted in favor of producing an adaptive version of WRF-ARW, including the hybrid LES/RANS model. as noted in the introduction, the primary code developer, Dr. Xiao, left the project just as work began on the WRF version. Due to few current doctoral graduates with CFD code development skills, compounded by visa restrictions for some candidates, it required eleven months to find a qualified replacement for Dr. Xiao. Because of this, the WRF version was not completed by project end. However, the development is being continued under separate DOD funding and will therefore be available for operational use when completed.

References

[1]Xiao, X., McRae, D. S., and Hassan, H. A., "Dynamically Resolved Simulation of Atmospheric Features and Turbulence-Initial Results," AIAA Paper 2005-0265, January 2005.

[2]Xiao, X., McRae, D. S., Hassan, H. A., Ruggiero, F. H., and Jumper, G. Y., "Modeling Atmospheric Optical Turbulence," AIAA Paper 2006–0077, January 2006.

[3]Xiao, X., McRae, D. S., and Hassan, H. A., "Role of Grid Adaptation in Optical Turbulence Prediction," AIAA Paper 2007-0083, January 2007.

[4]Xiao, X., McRae, D. S., Hassan, H. A., Jumper, G. Y., Ruggiero, F. H., and Jackson, A. J., "New Approach for Modeling Atmospheric Optical Turbulence," *AIAA Journal*, In Press, 2009.

[5]Jumper, G. Y. and Beland, R. R., "Progress in the Understanding and Modeling of Atmospheric Optical Turbulence," AIAA Paper 2000-2355, January 2000.

[6]Grell, G. A., Dudhia, J., and Stauffer, D. R., "A Description of the Fifth Generation Penn State/NCAR Mesoscale Model (MM5)," NCAR tech. Note T/N-398+STR, Boulder, CO, 1995.

[7]Tatarskii, V. I., *The Effect of the Turbulent Atmosphere on Wave Propagation*, U.S. Department of Commerce, National Technical Information Service, 1971.

[8]Ishimaru, A., *Wave Propagation and Scattering in Random Media*, IEEE Press, New York, 1997.

[9]Beland, R. R., "Propagation through Atmospheric Optical Turbulence," *The Infrared and Electro-Optical Systems Handbook*, edited by F. G. Smith, Vol. 2, SPIE Engineering Press, Bellingham, WA, 1993, pp. 157–232.

[10]Dewan, E. M., Good, R. E., Beland, B., and Brown, J., "A Model for (Optical Turbulence) Profiles using Radiosonde Data," Phillips Laboratory Technical Report PL-TR-93-2043, AD-A279399, March 1993.

[11]Jackson, A., "Modified Dewan Optical Turbulence Parameterization," Air Force Research Laboratory AFRL-VS-HA-TR 2004-1116, AD-A432901, Hanscom AFB, MA, June 2004.

[12]Bougeault, P., Hui, C. D., Fleury, B., and Laurent, J., "Investigation of Seeing by Means of an Atmospheric Mesoscale Numerical Simulation," *Applied Optics*, Vol. 34, No. 18, 1995, pp. 3481–3487.

[13]Tunick, A., "CN2 Model to Calculate the Micrometeorologocal Influences on the Refractive Index Structure Paramemter," *Environmental Modeling & Software*, Vol. 18, 2003, pp. 165–171.

[14]Robinson, D. F. and Hassan, H. A., "Further Development of the k-ζ (Enstrophy) Turbulence Closure Model," *AIAA Journal*, Vol. 39, No. 7, 1998, pp. 1825–1833.

[15]Xiao, X., Hassan, H. A., Edwards, J. R., and Gaffney Jr., R. L., "Role of Turbulent Prandtl Number on Heat Flux at Hypersonic Mach Number," *AIAA Journal*, Vol. 45, No. 4, 2007, pp. 806–813.

[16]Xiao, X., Edwards, J. R., and Hassan, H. A., "Blending Functions in Hybrid Large-Eddy/Reynolds-Averaged Navier-Stokes Simulations," *AIAA Journal*, Vol. 42, No. 12, 2004, pp. 2508–2515.

[17]Arakawa, A. and Lamb, V. R., "Computational Design of the Basic Dynamical Processes of the UCLA General Circulation Model," *Methods in Computational Physics*, Vol. 17, 1977, pp. 173–265.

[18]Cormen, T. H., Leiserson, C. E., Rivest, R. L., and Stein, C., *Introduction to Algorithms*, The MIT Press, Cambridge, MA, 2nd ed., 2001.

[19]Shu, C.-W., "Essential Non-Oscllatory and Weighted Essentially Non-Oscillatory Schemes for Hyperbolic Conservation Laws," ICASE Report 97-65, 1997, NASA/CR-97-206253.

[20] Rider, W. J., Greenough, J. A., and Kamm, J. R., "Combining High-order Accuracy with Non-Oscillatory Methods through Monotonicity Preservation," *International Journal for Numerical Methods in Fluids*, Vol. 47, 2005, pp. 1253–1259.

[21] Collela, P. and Woodward, P. R., "The Piecewise Parabolic Method (PPM) for gas-dynamical simulations," *Journal of Computational Physics*, Vol. 54, 1984, pp. 174–201.

[22] Yoshizawa, A. and Horiuti, K., "A Statistically-Derived Subgrid Scale Kinetic Energy Model for Large Eddy Simulation of Turbulent Flows," *Journal of Physical Society of Japan*, Vol. 54, 1985, pp. 2834–2839.

[23] Garratt, J. R., *The Atmospheric Boundary Layer*, Cambridge Atmospheric and Space Science Series, Cambridge University Press, Cambridge, UK, 1994.

[24] Ruggiero, F. H. and DeBenedicts, D. A., "Forecasting Optical Turbulence from Mesoscale Weather Prediction Models," Preprints, HPCMP Users Group Conference, Austin, TX, June 10–14 2002.

Appendix: Turbulence Model Equations

k-Equation:

$$
\begin{aligned}
\frac{\partial}{\partial t}(\bar{\rho}k) + \frac{\partial}{\partial x_j}(\bar{\rho}\tilde{u}_j k) =\ & \frac{\partial}{\partial x_j}\left[\left(\frac{\mu}{3} + \frac{\mu_t}{\sigma_k}\right)\frac{\partial k}{\partial x_j}\right] + \tau_{ij}\frac{\partial \tilde{u}_i}{\partial x_j} \\
& - (1 - \Gamma)\left(\frac{1}{C_k}\frac{\mu_t}{\bar{\rho}}\frac{\partial \bar{\rho}}{\partial x_i}\frac{\partial \bar{P}}{\partial x_i} + C_1\frac{\bar{\rho}k}{\tau_\rho} + \mu\zeta\right) - \Gamma C_d\bar{\rho}\frac{k^{3/2}}{\Delta} \qquad \text{(A.1)} \\
& + \frac{\bar{\rho}}{\tilde{\theta}}\left[g\delta_{i3} + 2\Omega_0\epsilon_{ijk}\eta_j\tilde{u}_k\right]\widetilde{\theta''u_i''}
\end{aligned}
$$

where the δ_{ij} is Kronecker Delta, Ω_0 is the magnitude of the angular velocity of the earth and ϵ_{ijk} is the permutation tensor.

ζ–Equation:

$$
\begin{aligned}
\frac{\partial}{\partial t}(\bar{\rho}\zeta) + \frac{\partial}{\partial x_j}(\bar{\rho}\tilde{u}_j\zeta) =\ & \frac{\partial}{\partial x_j}\left[\left(\mu + \frac{\mu_t}{\sigma_\zeta}\right)\frac{\partial \zeta}{\partial x_j}\right] \quad + \frac{\mu_t}{\sigma_r}\frac{\partial \Omega_i}{\partial x_j}\left(\frac{\partial \Omega_i}{\partial x_j} + \frac{\partial \Omega_j}{\partial x_i}\right) \\
& - \epsilon_{mij}\bar{\rho}\frac{\partial \Omega_i}{\partial x_j}\left[\frac{\partial}{\partial x_n}(\widetilde{u_m''u_n''}) - \frac{\partial k}{\partial x_m}\right] \quad + \left(a_3 b_{ij} + \frac{1}{3}\delta_{ij}\right)\bar{\rho}\zeta S_{ij} - \frac{\beta_5}{R_k + \delta}\bar{\rho}\zeta^{3/2} \\
& - \frac{2\beta_6\tau_{ij}\nu_t}{k\nu}\Omega\Omega_i\Omega_j + \frac{\beta_7\bar{\rho}\zeta}{\Omega^2}\Omega_i\Omega_j S_{ij} \quad + 2\beta_8\epsilon_{ilm}\left(\frac{\tau_{ij}}{k}\right)\frac{\partial k}{\partial x_l}\frac{\partial \zeta}{\partial x_m}\frac{\Omega_j}{S^2 + \Omega^2/2} \qquad \text{(A.2)} \\
& + \max(P_\zeta, 0) - 2\bar{\rho}\zeta S_{ii} - C_{\zeta,0}\frac{\mu_t\zeta\Omega}{\tau_\rho k} \quad - C_{\zeta,1}g\Omega_3\sqrt{\left(\frac{\partial \bar{\rho}}{\partial x_i}\right)^2} + C_{\zeta,2}\Omega\eta_j\sqrt{k}\frac{\partial \tilde{u}_l}{\partial x_j}\frac{\partial \bar{\rho}}{\partial x_l} \\
& + 2\Omega_0 C_{\zeta,3}\bar{\rho}\eta_j\Omega_j\sqrt{\zeta}
\end{aligned}
$$

where

$$S_{ij} = \frac{1}{2}\left(\frac{\partial \tilde{u}_i}{\partial x_j} + \frac{\partial \tilde{u}_j}{\partial x_i}\right) \tag{A.3}$$

$$\Omega_i = \epsilon_{ijk}\frac{\partial \tilde{u}_k}{\partial x_j}; \quad \Omega^2 = \Omega_i\Omega_i \tag{A.4}$$

$$\nu_t = \frac{\mu_t}{\bar{\rho}} = (1 - \Gamma)\nu_{t,RANS} + \Gamma\nu_{t,LES} \tag{A.5}$$

$$\nu_{t,RANS} = C_\mu\frac{k^2}{\nu\zeta} \tag{A.6}$$

$$\nu_{t,LES} = C_s\sqrt{k}\Delta \tag{A.7}$$

$$\Gamma = \tanh\left(\frac{l_\epsilon}{\alpha_1\Delta}\right)^2 \tag{A.8}$$

$$l_\epsilon = \frac{k^{3/2}}{\nu\zeta} \tag{A.9}$$

$$b_{jk} = \frac{\tau_{jk}}{\bar{\rho}k} + \frac{2}{3}\delta_{jk} \tag{A.10}$$

$$\vec{\eta} = [0, \cos\phi, \sin\phi]; \quad \phi \text{ is the latitude} \tag{A.11}$$

Potential Temperature Variance ($\widetilde{\theta''^2}$) Equation:

$$\frac{\partial}{\partial t}(\bar{\rho}\widetilde{\theta''^2}/2) + \frac{\partial}{\partial x_j}(\bar{\rho}\tilde{u}_j\widetilde{\theta''^2}/2) = \frac{\partial}{\partial x_j}\left[\bar{\rho}\left(\gamma\alpha + C_{h,2}\alpha_t\right)\frac{\partial(\widetilde{\theta''^2}/2)}{\partial x_j}\right]$$

$$-q_{t,j}\frac{\partial\tilde{\theta}}{\partial x_j} + 2\frac{\mu\gamma S_{ij}}{C_p}\left[\frac{\partial}{\partial x_j}\left(\frac{q_{t,i}}{\bar{\rho}}\right) + \frac{\partial}{\partial x_i}\left(\frac{q_{t,j}}{\bar{\rho}}\right)\right]$$

$$-\frac{4}{3}\mu\gamma S_{kk}\frac{\partial}{\partial x_j}\left(\frac{q_{t,j}}{\bar{\rho}}\right) \quad -(\gamma-1)\bar{\rho}\widetilde{\theta''^2}\frac{\partial\tilde{u}_i}{\partial x_i} - (1-\Gamma)\gamma\bar{\rho}\epsilon_\theta$$

$$-\Gamma C_{h,d}\bar{\rho}\frac{\widetilde{\theta''^2}^{5/4}\sqrt{C_p}}{\Delta} + 2C_{h,4}\gamma\frac{\mu}{C_p}\sqrt{\widetilde{\theta''^2}}\zeta \tag{A.12}$$

where

$$q_{t,j} \equiv \overline{\rho u_j'' \theta''} = -\bar{\rho} \left(\alpha_t \frac{\partial \tilde{\theta}}{\partial x_j} + C_{h,g} \frac{\tau_h g}{\tilde{\theta}} \delta_{j3} \widetilde{\theta''^2} \right) \tag{A.13}$$

$$\alpha_t = (1 - \Gamma)\alpha_{t,RANS} + \Gamma \alpha_{t,LES} \tag{A.14}$$

$$\alpha_{t,RANS} = \frac{1}{2} \left(C_{h,1} k \tau_\theta + \nu_{t,RANS}/0.89 \right) \tag{A.15}$$

$$\alpha_{t,LES} = \frac{1}{2} \left(C_{h,t} \sqrt{C_p} \left(\widetilde{\theta''^2} \right)^{1/4} \Delta + \nu_{t,LES}/0.89 \right) \tag{A.16}$$

$$\tau_h = \widetilde{\theta''^2}/\epsilon_{\theta,hybrid} \tag{A.17}$$

$$\tau_\theta = \widetilde{\theta''^2}/\epsilon_\theta \tag{A.18}$$

and C_p is the specific heat of constant pressure.

Equation for the Dissipation Rate of Potential Temperature Variance:

$$\frac{\partial}{\partial t}(\bar{\rho}\epsilon_\theta) + \frac{\partial}{\partial x_j}(\bar{\rho}\tilde{u}_j \epsilon_\theta) = \frac{\partial}{\partial x_j} \left[(\gamma \bar{\rho}\alpha + C_{h,7}\mu_t) \frac{\partial \epsilon}{\partial x_j} \right] - \bar{\rho}\epsilon_\theta \left(C_{h,5} b_{jk} - \frac{\delta_{jk}}{3} \right) \frac{\partial \tilde{u}_j}{\partial x_k}$$
$$+ C_{h,6}\bar{\rho}k \frac{\partial \sqrt{\widetilde{\theta''^2}}}{\partial x_j} \frac{\partial \tilde{\theta}}{\partial x_j} - C_{h,8}\frac{q_{t,j}}{\tau_h} \frac{\partial \tilde{\theta}}{\partial x_j} - \gamma \bar{\rho}\epsilon_\theta \left(\frac{C_{h,9}}{\tau_\theta} + \frac{C_{h,10}}{\tau_k} \right) \tag{A.19}$$

where

$$\tau_k = \frac{k}{\nu \zeta} \tag{A.20}$$

Model Constants

The constants in the model equations are given below:

Location	Model Constant	Value
k-equation	σ_k	1.8
	C_k	2.0
	C_1	0.6
ζ-equation	σ_ζ	1.4
	σ_r	0.07
	a_3	0.35
	δ	0.01
	β_5	2.37
	β_6	0.10
	β_7	1.50
	β_8	2.3
	$C_{\zeta,0}$	0.0
	$C_{\zeta,1}$	1.0
	$C_{\zeta,2}$	0.0
	$C_{\zeta,3}$	0.0
$\nu_{t,RANS}$	C_μ	0.09
$\nu_{t,LES}$	C_s	0.01
Γ	α_1	10^{-5}
$q_{t,j}$	$C_{h,g}$	-1.0
$\alpha_{t,LES}$	$C_{h,t}$	10^{-4}
$\alpha_{t,RANS}$	$C_{h,1}$	0.0648
$\widetilde{\theta''^2}$-equation	$C_{h,2}$	0.50
	$C_{h,4}$	-0.4
	$C_{h,d}$	2.5×10^{-4}
ϵ_θ-equation	$C_{h,5}$	-0.05
	$C_{h,6}$	-0.12
	$C_{h,7}$	1.45
	$C_{h,8}$	0.76
	$C_{h,9}$	0.87
	$C_{h,10}$	0.25
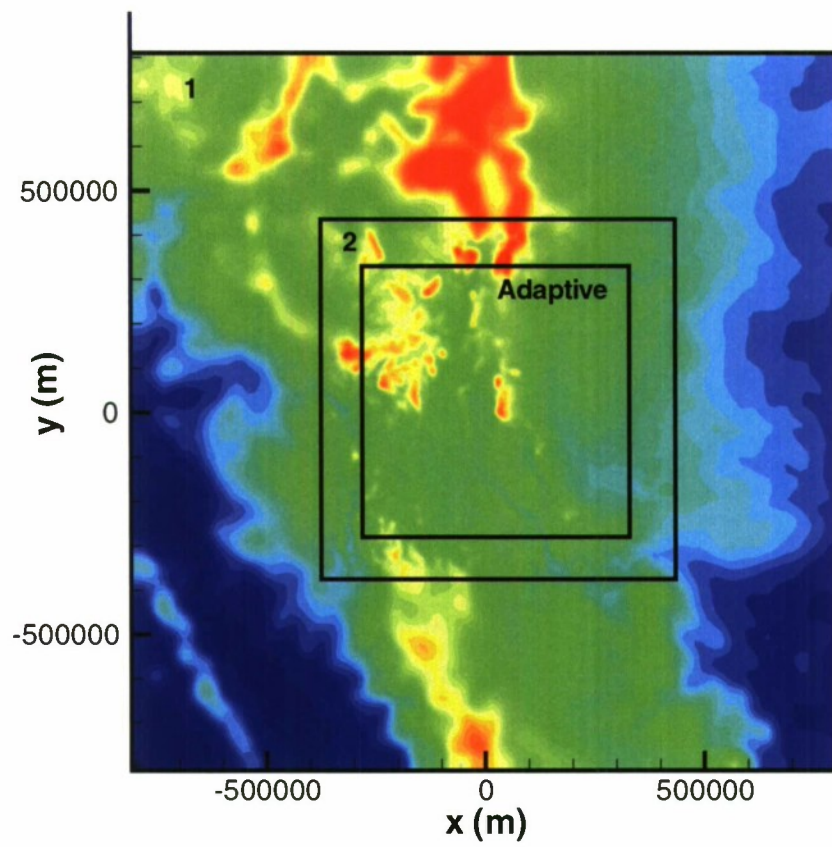
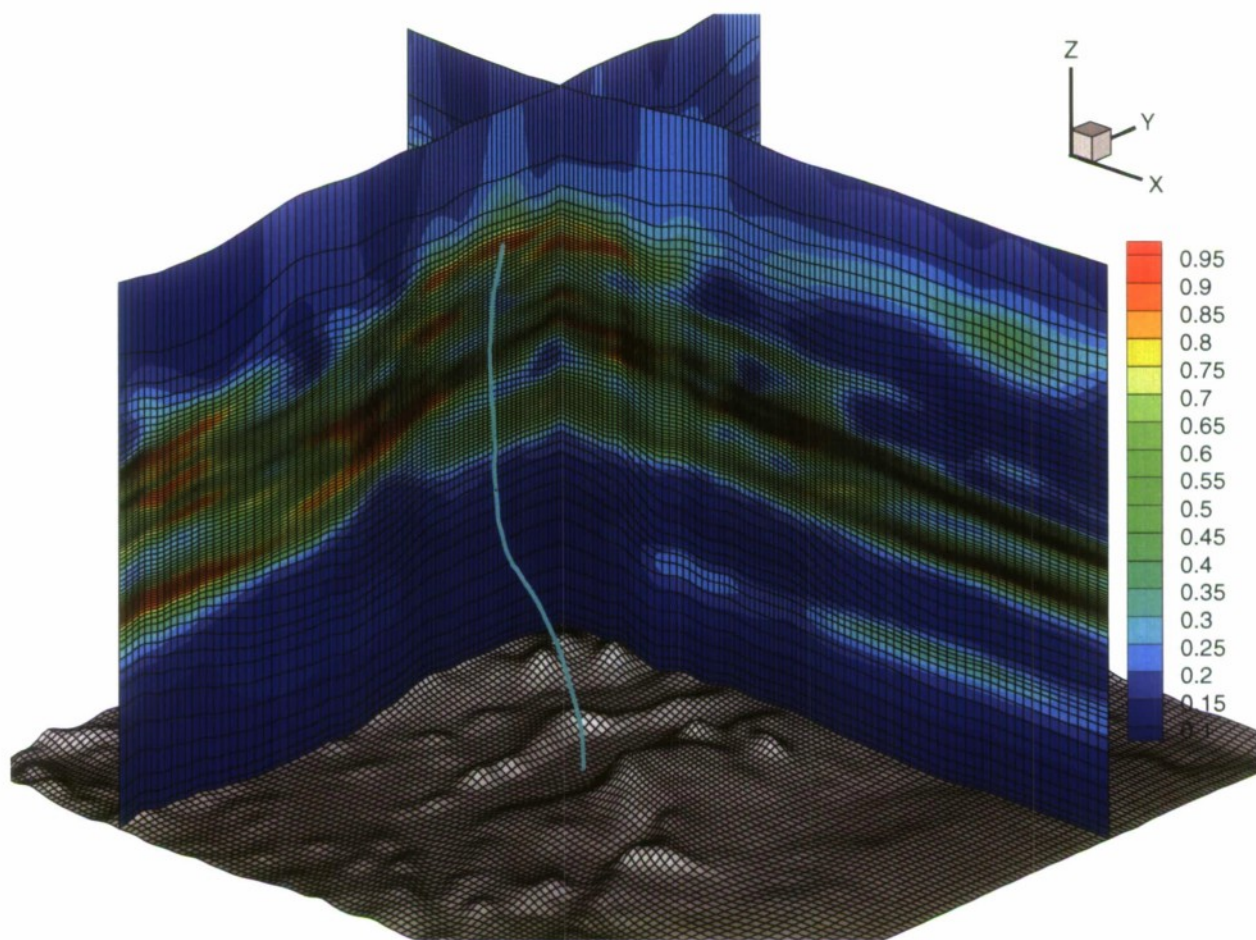Figure 1. Domain layout with terrain elevation contours.

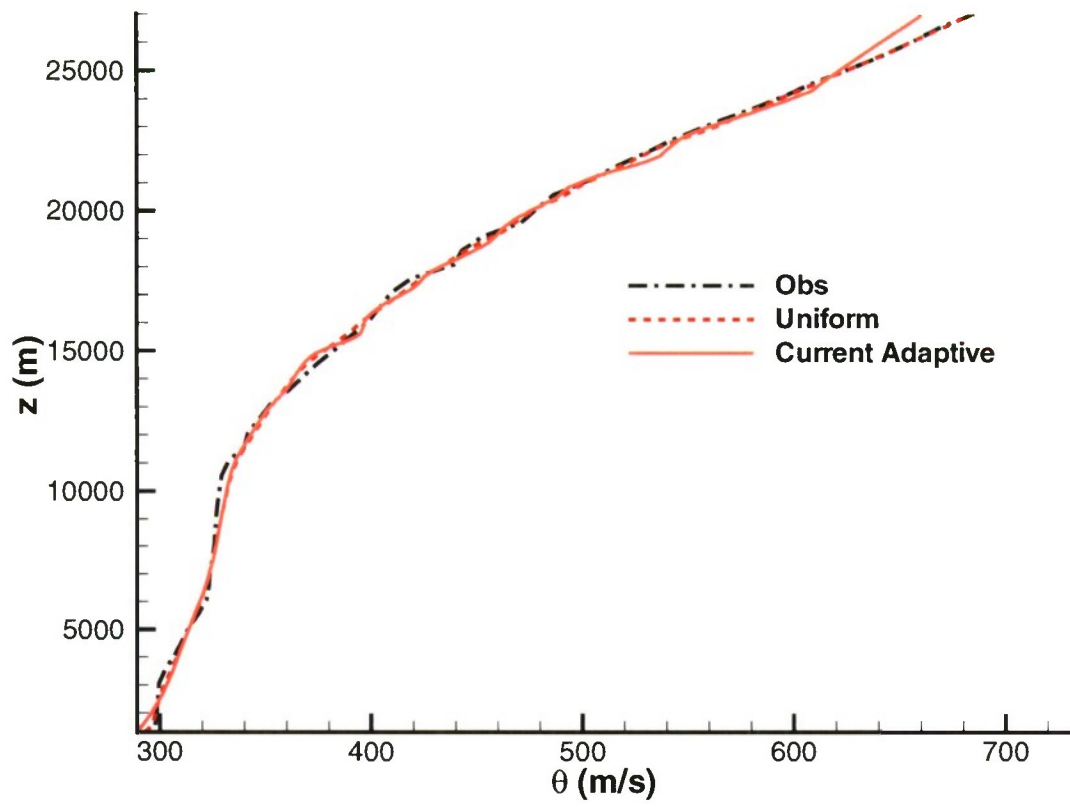Figure 2. Adaptive grid with weight function contours and balloon trajectory

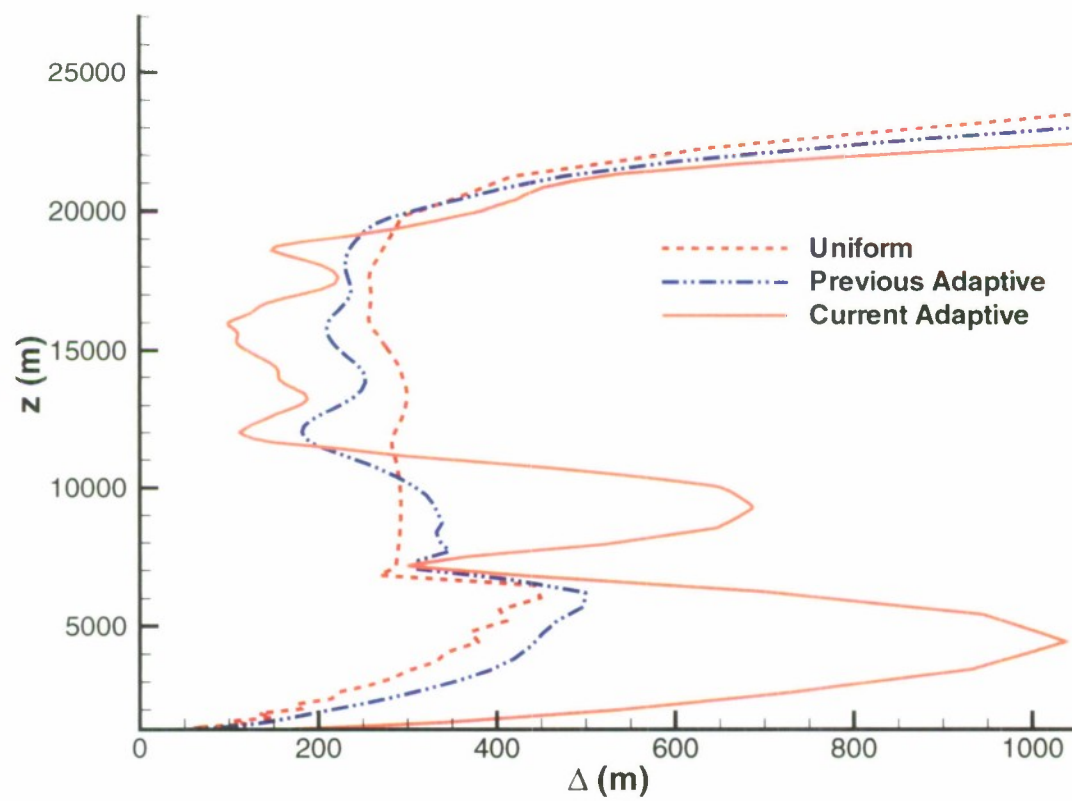Figure 3. Comparison of potential temperature profiles.

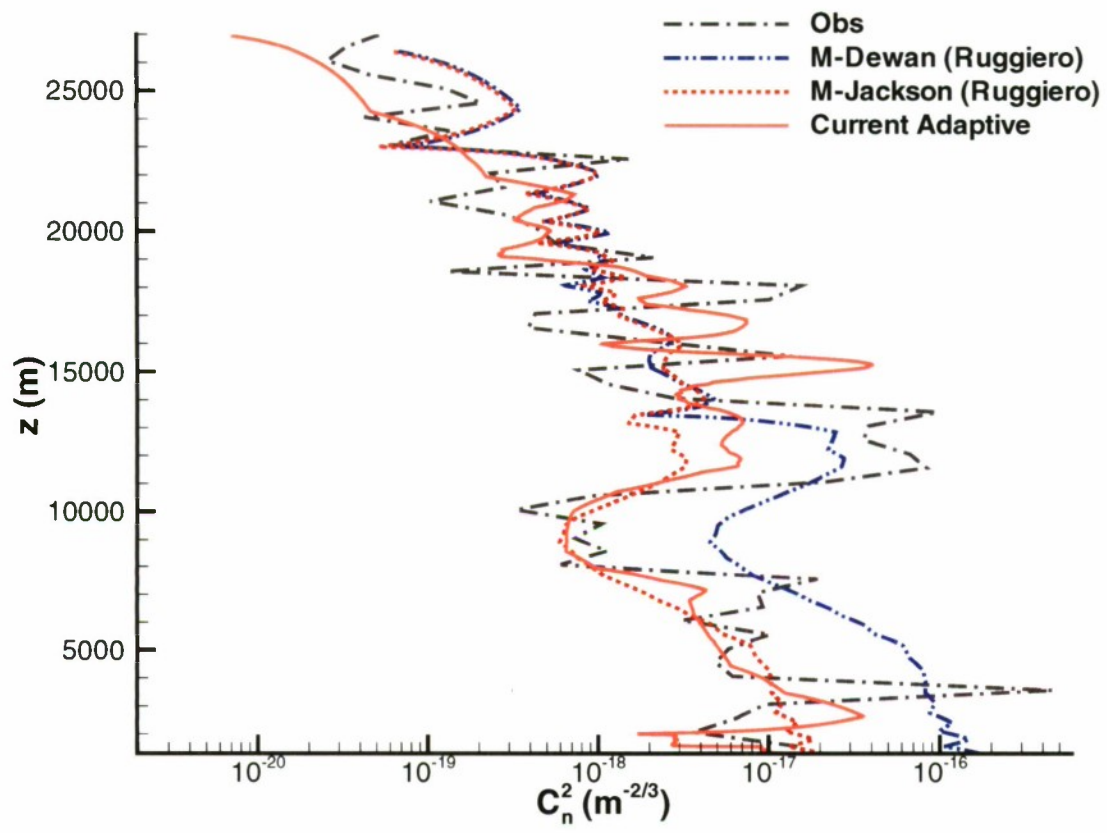Figure 4. Comparison of mesh spacing profiles.
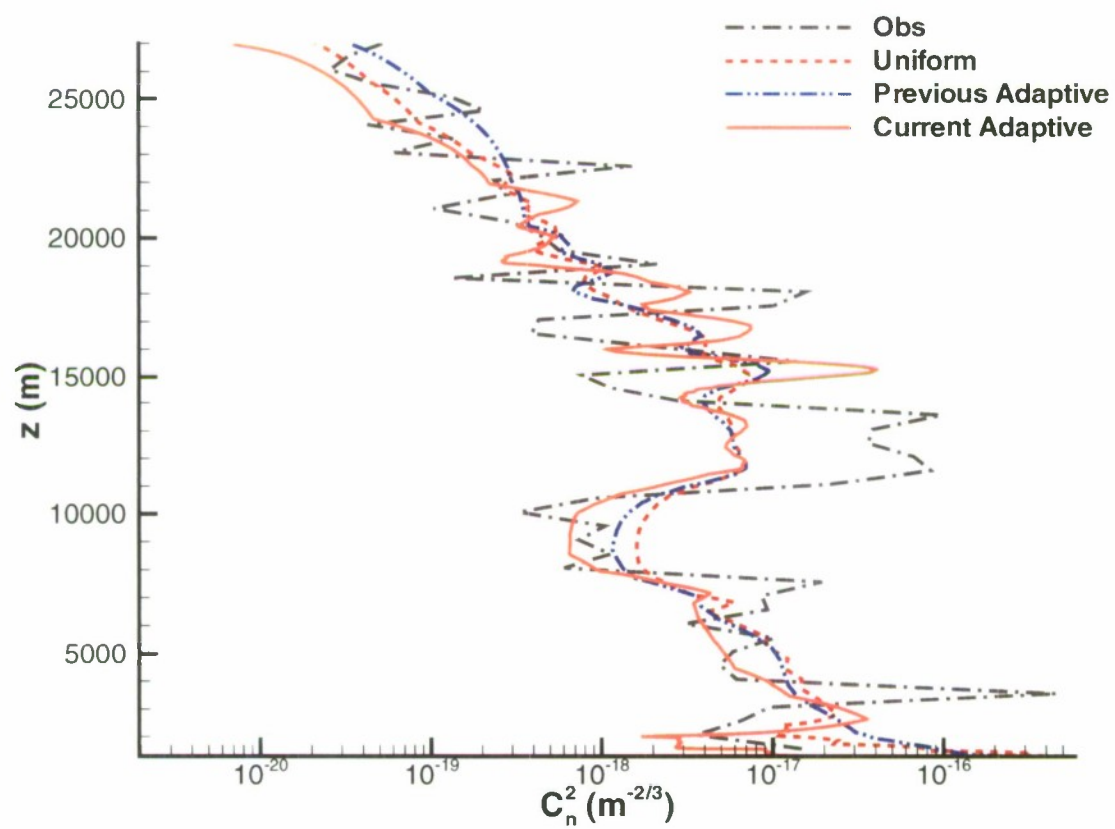
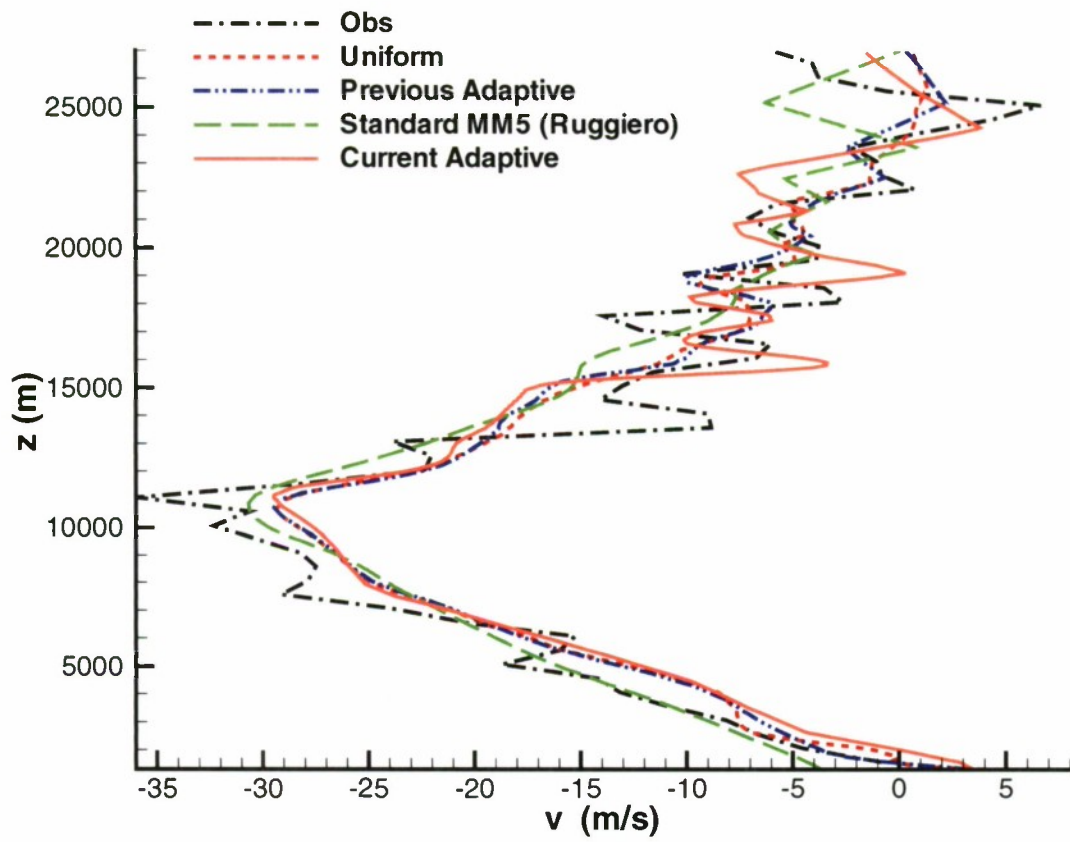Figure 5. Comparison of C_n^2 profiles.

Figure 6. Comparison of C_n^2 profiles.

Figure 7. Comparison of meridional wind profiles